

Navigation With Differential Carrier Phase Measurements From Megaconstellation LEO Satellites

Joe Khalife*, Mohammad Neinavaie†, and Zaher M. Kassas*†
University of California, Irvine, U.S.A.

* Department of Mechanical and Aerospace Engineering

† Department of Electrical Engineering and Computer Science

Email: khalifej@uci.edu, mneinava@uci.edu, zkassas@ieee.org

Abstract—An opportunistic framework to navigate with differential carrier phase measurements from megaconstellation low Earth orbit (LEO) satellite signals is proposed. A computationally efficient integer ambiguity resolution algorithm is proposed to reduce the size of the integer least-squares (ILS) problem, whose complexity grows exponentially with the number of satellites. The Starlink constellation is used as a specific megaconstellation example to demonstrate the efficacy of the proposed algorithm, showing a 60% reduction in the size of the ILS problem. The joint probability density function of the megaconstellation LEO satellites’ azimuth and elevation angles is derived for efficient and accurate performance characterization of navigation frameworks with LEO satellites, and to facilitate system parameter design to meet desired performance requirements. Experimental results are presented showing an unmanned aerial vehicle (UAV) navigating for 2.28 km exclusively using signals from only two Orbcomm LEO satellites via the proposed framework, achieving an unprecedented position root mean squared error of 14.8 m over a period of 2 minutes.

Index Terms—LEO, megaconstellation, differential carrier phase, navigation, real time kinematic (RTK).

I. INTRODUCTION

The coming decade is slated to witness a space revolution with the launch of tens of thousands of low Earth orbit (LEO) satellites for broadband communication [1]. The promise of utilizing LEO satellites for navigation and timing has been the subject of recent studies [1]–[5]. While some of these studies call for tailoring the broadband protocol to support navigation capabilities [1], [6], other studies propose to exploit existing broadband LEO constellations for navigation in an opportunistic fashion [3]–[5], [7]–[9]. The former studies allow for simpler receiver architectures and navigation algorithms. However, they require significant changes to existing infrastructure, the cost of which private companies such as OneWeb, SpaceX, Boeing, and others, which are planning to aggregate launch tens of thousands of broadband Internet satellites into LEO, may not be willing to pay. Moreover, if the aforementioned companies agree to that additional cost, there will be no guarantees that they would not charge for

“extra navigation services.” In this case, exploiting broadband LEO satellite signals opportunistically for navigation becomes the more viable approach. This paper assesses opportunistic navigation with differential carrier phase measurements from broadband LEO satellite signals.

To address the limitations and vulnerabilities of global navigation satellite system (GNSS), opportunistic navigation has received significant attention over the past decade or so [10]–[12]. Opportunistic navigation is a paradigm that relies on exploiting ambient radio signal of opportunity (SOPs) for positioning and timing [13]. Besides LEO satellite signals, other SOPs include AM/FM radio [14]–[16], digital television [17], [18], WiFi [19], [20], and cellular [21]–[27], with the latter showing the promise of a submeter-accurate navigation solution for unmanned aerial vehicles (UAVs) when carrier phase measurements from cellular signals are used [28]–[30].

LEO satellites possess desirable attributes for positioning in GNSS-challenged environments: (i) they are around twenty times closer to Earth compared to GNSS satellites, which reside in medium Earth orbit (MEO), making their received signal power between 24 to 34 dBs higher than GNSS signals; (ii) they will become abundant as tens of thousands of broadband Internet satellites are expected to be deployed into LEO [1]; and (iii) each broadband provider will deploy broadband Internet satellites into unique constellations, transmitting at different frequency bands, making LEO satellite signals diverse in frequency and direction [31]. Moreover, the Keplerian elements parameterizing the orbits of these LEO satellites are made publicly available by the North American Aerospace Defense Command (NORAD) and are updated daily in the two-line element (TLE) files. Using TLEs and orbit determination algorithms (e.g., SGP4), the positions and velocities of these satellites can be known, albeit not precisely. In addition, some of these broadband LEO satellites, such as Orbcomm satellites, are equipped with GPS receivers and broadcast their GPS solution to terrestrial receivers.

This paper considers the problem of navigating exclusively with LEO satellite signals in environments where GNSS signals are unavailable or untrustworthy. To this end, there are several challenges that must be overcome. First, there

This work was supported in part by the Office of Naval Research (ONR) under Grant N00014-19-1-2511 and in part by the National Science Foundation (NSF) under Grant 1929965.

are no publicly available receivers that can produce navigation observables from LEO satellite signals. Second, existing navigation frameworks do not apply in a straight forward fashion to megaconstellation LEO satellites due to the unique error sources associated with megaconstellation LEO satellites. Third, the achievable navigation performance with megaconstellation LEO satellites is not fully characterized. The first two challenges have been partially addressed for Orbcomm satellite signals [8], [32]. This paper makes four contributions that aim to address the aforementioned second and third challenges:

- First, a carrier phase differential (CD)-LEO navigation framework is developed for real broadband LEO satellite signals and an efficient method for resolving carrier phase integer ambiguities in a batch solver is proposed. The performance and complexity of the proposed integer ambiguity resolution method are also characterized.
- Second, the probability density functions (pdfs) of megaconstellation LEO satellites' azimuth and elevation angles are derived. These pdfs are essential tools to efficiently study the performance of LEO satellite-based navigation.
- Third, the performance of the CD-LEO framework is characterized using the derived pdfs by analyzing (i) the position dilution of precision (PDOP) of megaconstellation LEO satellites, (ii) the measurement residuals due to ephemeris errors, and (iii) the measurement residuals due to integer ambiguity estimation errors as a function of the system design parameters, more precisely, the differential baseline and the batch size. This study allows to design the system parameters to guarantee a desired performance.
- Fourth, novel experimental results are presented showing an unmanned aerial vehicle (UAV) localizing itself with real LEO satellite signals using differential carrier phase measurements to an acceptable level of accuracy.

The high level of precision of carrier phase measurements enables a sub-meter level navigation solution as has been demonstrated in GNSS [33] and cellular SOPs [28]–[30]. However, this precision comes at the cost of added ambiguities that need to be resolved. This paper addresses this challenge for megaconstellation LEO satellites. Consider a receiver onboard a “rover” on Earth making carrier phase measurements to broadband LEO satellites and a “base” station in the vicinity of the rover making carrier phase measurements to the same LEO satellites. One can form the double-difference carrier phase measurements from base and rover measurements and solve for the rover’s position as well as for the resulting integer ambiguities. Without any position priors, the rover cannot perform real-time positioning and must wait until there is enough change in satellite geometry and solve a batch least-squares to estimate its position and the integer ambiguities [34]. To optimally resolve the integer ambiguities, an integer least-squares (ILS) estimator can be employed. However, the complexity of the ILS grows exponentially with the number of ambiguities [35]. With the proposed LEO constellations, hundreds of satellites are expected to be visible at any point

in time and almost anywhere on Earth, making the ILS approach infeasible. To address this issue, this paper proposes an integer ambiguity resolution algorithm that approaches the performance of the ILS but with the fraction of its complexity. Once the ambiguities are resolved, the rover can perform real-time positioning.

Aside from integer ambiguities, another major source of error that has to be considered in the CD-LEO framework is the error in the satellite positions obtained from the TLE files. These errors can be on the order of kilometers as the orbit is propagated way beyond the epoch at which the TLE file was generated. Blindly using the satellite positions obtained from the TLE files introduces significant errors in the measurement residuals. Although the double-difference carrier phase measurements will cancel out most of these errors, there will still be significant errors if the base and rover are “too far apart”. These errors are too large to ignore if an accurate navigation solution is desired. This paper characterizes this error and its statistics as a function of the differential baseline, from which the baseline can be designed to guarantee a desirable performance.

The performance of the proposed integer ambiguity resolution algorithm and the magnitude of the CD-LEO measurement residuals due to ephemeris errors heavily depend on the satellite-to-receiver geometry, which is captured by the satellites’ azimuth and elevation angles. Subsequently, it is of paramount importance to characterize the distribution of these angles for LEO megaconstellations. While previous work approximate the angles’ marginal distributions or study the elevation angle distribution for small constellations [36], [37], this paper characterizes the full joint distribution of the azimuth and elevation angles for LEO megaconstellation satellites. This characterization enables several efficient and insightful performance analyses, as well as facilitates performance-driven framework design, i.e., design system parameters to meet desired performance requirements.

The paper is organized as follows. Section II describes the models used, the CD-LEO framework, and the proposed integer ambiguity resolution algorithm. Section III derives the joint pdf of the megaconstellation LEO satellites’ azimuth and elevation angles. Section IV uses these models to characterize the performance of the CD-LEO framework and proposes a methodology to design system parameters to meet a desired performance. Section V presents experimental results demonstrating a UAV navigating with CD-LEO measurements. Concluding remarks are given in Section VI.

II. MODELS AND CD-LEO FRAMEWORK DESCRIPTION

This section describes the models and the CD-LEO framework used in the paper. Note that in the sequel, a satellite will be referred to as a space vehicle (SV).

A. LEO Satellite Position Error

Let $\mathbf{r}_{1\text{eol}} \triangleq [x_{1\text{eol}}, y_{1\text{eol}}, z_{1\text{eol}}]^T$ denote the l -th LEO SV true position vector in the East-North-Up (ENU) frame. If the true LEO SV positions are not known, they may be estimated

utilizing TLE files and orbit determination algorithms (e.g., SGP4), resulting with an estimate $\hat{\mathbf{r}}_{\text{leo}_l}$. Denote the estimation error as $\tilde{\mathbf{r}}_{\text{leo}_l} \triangleq \mathbf{r}_{\text{leo}_l} - \hat{\mathbf{r}}_{\text{leo}_l}$. Due to the large ephemeris errors in TLE files, $\|\tilde{\mathbf{r}}_{\text{leo}_l}\|_2$ can be on the order of a few kilometers, with most of the error being in the along-track coordinate. To illustrate this, the position error of 2 Orbcomm LEO SVs, FM 108 and FM 116, is calculated by differencing (i) the LEO SVs' position estimate obtained from on-board GPS receivers and broadcasted in the Orbcomm message and (ii) the estimates obtained from TLE files and SGP4 software. The total SV position error magnitude $\|\tilde{\mathbf{r}}_{\text{leo}_l}\|_2$ for each SV and the along-track SV position error magnitude are shown in Fig. 1. Fig. 1 also shows the range residual due to ephemeris errors as observed by a terrestrial LEO receiver, i.e., it is the difference between (i) the true range between the LEO SV and LEO receiver and (ii) the range estimated using the LEO position estimated obtained from TLE files. It can be seen from Fig. 1 that (i) the SV position error can be significant (around 5 km for FM 116), (ii) most of the error is in the along-track direction, and (iii) the range residual is on the order of the SV position error. In order to reduce the effect of ephemeris errors, a navigating vehicle can employ simultaneous tracking and navigation (STAN) framework to estimate the LEO SVs' states simultaneously with the vehicle's states [5], [38]. Alternatively, a reference receiver, or base, may be deployed to provide differential corrections, which will significantly reduce the range residuals. This reduction is characterized in Section IV as a function of the SV elevation and azimuth angles. The sequel describes the carrier phase measurement model and the CD-LEO framework.

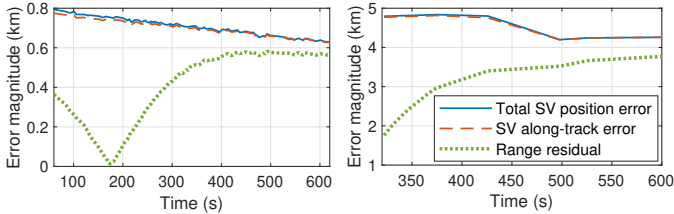


Fig. 1. Total SV position error magnitude and along-track SV position error magnitude for 2 Orbcomm LEO SVs, as well as the range residual due to ephemeris errors as observed by a terrestrial LEO receiver.

B. LEO Carrier Phase Observation Model

In this paper, availability of carrier phase measurements from LEO SV signals is assumed. For example, the receiver proposed in [8] may be used to obtain carrier phase measurements from Orbcomm LEO SV signals. Note that since LEO satellite orbits are above the ionosphere, their signals will suffer from ionospheric and tropospheric delays. Let $\delta t_{\text{iono},l}^{(i)}(k)$ and $\delta t_{\text{trop},l}^{(i)}(k)$ denote the ionospheric and tropospheric delays from the l -th LEO SV to the i -th receiver at time-step k , respectively, where i denotes either the base B or the rover R. An estimate of the ionospheric and tropospheric delays, denoted $\hat{\delta} t_{\text{iono},l}^{(i)}(k)$ and $\hat{\delta} t_{\text{trop},l}^{(i)}(k)$, respectively, may be obtained using standard models [34]. After ionospheric and tropospheric delay correction, the carrier phase measurement

$z_l^{(i)}(k)$ expressed in meters can be parameterized in terms of the receiver and LEO SV states as

$$z_l^{(i)}(k) = \|\mathbf{r}_{r_i} - \mathbf{r}_{\text{leo}_l}(k)\|_2 + c[\delta t_{r_i}(k) - \delta t_{\text{leo}_l}(k)] + \lambda_l N_l^{(i)} + c\tilde{\delta} t_{\text{trop},l}^{(i)}(k) + c\tilde{\delta} t_{\text{iono},l}^{(i)}(k) + v_l^{(i)}(k), \quad (1)$$

where $\mathbf{r}_{r_i} \triangleq [x_{r_i}, y_{r_i}, z_{r_i}]^T$ is the i -th receiver's position vector in ENU; c is the speed of light; δt_{r_i} and δt_{leo_l} are the i -th receiver's and l -th LEO SV clock biases, respectively; $\tilde{\delta} t_{\text{iono},l}^{(i)}(k) \triangleq \delta t_{\text{iono},l}^{(i)}(k) - \hat{\delta} t_{\text{iono},l}^{(i)}(k)$ and $\tilde{\delta} t_{\text{trop},l}^{(i)}(k) \triangleq \delta t_{\text{trop},l}^{(i)}(k) - \hat{\delta} t_{\text{trop},l}^{(i)}(k)$ are the ionospheric and tropospheric delay errors, respectively; λ_l is the l -th LEO SV signal's wavelength; $N_l^{(i)}$ is the carrier phase ambiguity; and $v_l^{(i)}(k)$ is the measurement noise, which is modeled as a discrete-time zero-mean white Gaussian sequence with variance $[\sigma_l^{(i)}(k)]^2$. It is assumed that $\{v_l^{(i)}\}_{l=1}^L$ are independent and identically distributed, but with different values of $[\sigma_l^{(i)}(k)]^2$.

C. CD-LEO Framework

The framework consists of a rover and a base receiver in an environment comprising L visible LEO SVs. The base receiver (B), is assumed to have knowledge of its own position state, e.g., (i) a stationary receiver deployed at a surveyed location or (ii) a high-flying UAV with access to GNSS. The rover (R) does not have knowledge of its position. The base communicates its own position and carrier phase observables with the rover. The LEO SVs' positions are known through the TLE files and orbit determination software, or by decoding the transmitted ephemerides, if any. Fig. 2 illustrates the base/rover CD-LEO framework.

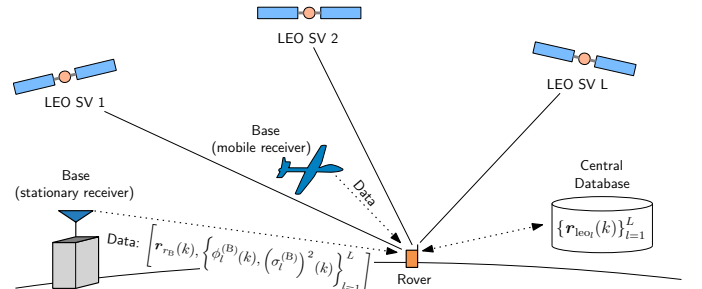


Fig. 2. Base/rover CD-LEO framework. The base receiver can be either (a) stationary or (ii) mobile (e.g., high-flying aerial vehicle).

In what follows, the objective is to estimate the rover's position using double difference carrier phase measurements. However, such measurements have inherent ambiguities that must be resolved. Recall that $(L - 1)$ measurements are obtained from L visible satellites [34], with one unknown ambiguity associated with each double difference measurement. Using only one set of carrier phase measurements with no *a priori* knowledge on the rover position results in an underdetermined system: $(L + 2)$ unknowns (3 position states and $(L - 1)$ ambiguities) with only $(L - 1)$ measurements. Therefore, when no *a priori* information on the position of the rover is

known, a batch weighted nonlinear least-squares (B-WNLS) over a window of K time-steps is employed to solve for the rover's position and ambiguities. The rover could either remain stationary or move during the batch window. Subsequently, the rover uses measurements collected at different times in a batch estimator, resulting in an overdetermined system [34]. The total number of measurements will be $K \times (L - 1)$ in the batch window. If the rover remains stationary, the total number of unknowns will remain $L+2$. Otherwise, the number of unknowns becomes $3K + L - 1$ (3 position states at each time-step and $(L - 1)$ ambiguities). The dimensions of the unknown parameters and the measurement vector set a necessary condition on K and L in order to obtain a solution. Once an estimate of the ambiguities is obtained, the rover position can be estimated in real-time using a point-solution weighted nonlinear least-squares (PS-WNLS) estimator. Both the B-WNLS and PS-WNLS estimate the rover's position from LEO double difference carrier phase measurements, which is described next.

D. LEO Double Difference Carrier Phase Observation Model

First, define the single difference across receivers adjusted for the base-LEO SV range as

$$\begin{aligned} z_l^{(R,B)}(k) &\triangleq z_l^{(R)}(k) - z_l^{(B)}(k) + \|\mathbf{r}_{r_B} - \hat{\mathbf{r}}_{\text{leo}_l}(k)\|_2 \\ &= \|\mathbf{r}_{r_R} - \mathbf{r}_{\text{leo}_l}(k)\|_2 + c\delta t_r^{(R,B)}(k) + \lambda_l N_l^{(R,B)} \\ &\quad + c\tilde{\delta}t_{\text{iono},l}^{(R,B)}(k) + c\tilde{\delta}t_{\text{trop},l}^{(R,B)}(k) \\ &\quad - \tilde{r}_{\text{leo}_l}^{(B)}(k) + v_l^{(R,B)}(k), \end{aligned} \quad (2)$$

where

$$\begin{aligned} \delta t_r^{(R,B)}(k) &\triangleq \delta t_{r_R}(k) - \delta t_{r_B}(k), \\ \lambda_l N_l^{(R,B)} &\triangleq \lambda_l N_l^{(R)} - \lambda_l N_l^{(B)}, \\ \tilde{\delta}t_{\text{iono},l}^{(R,B)}(k) &\triangleq \tilde{\delta}t_{\text{iono},l}^{(R)}(k) - \tilde{\delta}t_{\text{iono},l}^{(B)}(k), \\ \tilde{\delta}t_{\text{trop},l}^{(R,B)}(k) &\triangleq \tilde{\delta}t_{\text{trop},l}^{(R)}(k) - \tilde{\delta}t_{\text{trop},l}^{(B)}(k), \\ \tilde{r}_{\text{leo}_l}^{(B)}(k) &\triangleq \|\mathbf{r}_{r_B} - \mathbf{r}_{\text{leo}_l}(k)\|_2 - \|\mathbf{r}_{r_B} - \hat{\mathbf{r}}_{\text{leo}_l}(k)\|_2, \\ v_l^{(R,B)}(k) &\triangleq v_l^{(R)}(k) - v_l^{(B)}(k). \end{aligned}$$

It was observed from real data that $\tilde{\delta}t_{\text{iono},l}^{(R,B)}(k)$ and $\tilde{\delta}t_{\text{trop},l}^{(R,B)}(k)$ are negligible for VHF signals [32]. For higher frequency signals, this difference becomes even less significant as ionospheric delays decrease with the square of the carrier frequency [34]. Subsequently, $z_l^{(R,B)}(k)$ is approximated as

$$\begin{aligned} z_l^{(R,B)}(k) &\approx h_l^{(R)}(k) + c\delta t_r^{(R,B)}(k) + \lambda_l N_l^{(R,B)} \\ &\quad + \tilde{r}_{\text{leo}_l}^{(R,B)}(k) + v_l^{(R,B)}(k), \end{aligned} \quad (3)$$

where $h_l^{(R)}(k) \triangleq \|\mathbf{r}_{r_R} - \hat{\mathbf{r}}_{\text{leo}_l}(k)\|_2$, $\tilde{r}_{\text{leo}_l}^{(R,B)}(k) \triangleq \tilde{r}_{\text{leo}_l}^{(R)}(k) - \tilde{r}_{\text{leo}_l}^{(B)}(k)$, and $\tilde{r}_{\text{leo}_l}^{(R)}(k) \triangleq \|\mathbf{r}_{r_R} - \mathbf{r}_{\text{leo}_l}(k)\|_2 - \|\mathbf{r}_{r_R} - \hat{\mathbf{r}}_{\text{leo}_l}(k)\|_2$. In vector form, the measurement equation becomes

$$\mathbf{z}(k) \triangleq \mathbf{h}_R(k) + c\delta t_r^{(R,B)}(k)\mathbf{1}_L + \mathbf{A} + \tilde{\mathbf{r}}_{\text{leo}}^{(R,B)}(k) + \mathbf{v}(k), \quad (4)$$

where $\mathbf{1}_L$ is an $L \times 1$ vector of ones and

$$\begin{aligned} \mathbf{z}(k) &\triangleq [z_1^{(R,B)}(k), \dots, z_L^{(R,B)}(k)]^\top \\ \mathbf{h}_R(k) &\triangleq [h_1^{(R)}(k), \dots, h_L^{(R)}(k)]^\top \\ \mathbf{A} &\triangleq [\lambda_1 N_1^{(R,B)}, \dots, \lambda_L N_L^{(R,B)}]^\top \\ \tilde{\mathbf{r}}_{\text{leo}}^{(R,B)}(k) &\triangleq [\tilde{r}_{\text{leo}_1}^{(R,B)}(k), \dots, \tilde{r}_{\text{leo}_L}^{(R,B)}(k)]^\top \\ \mathbf{v}(k) &\triangleq [v_1^{(R,B)}(k), \dots, v_L^{(R,B)}(k)]^\top. \end{aligned}$$

The covariance matrix of $\mathbf{v}(k)$ is given by $\mathbf{R}(k) \triangleq \text{diag} \left[\left[\sigma_1^{(R,B)}(k) \right]^2, \dots, \left[\sigma_L^{(R,B)}(k) \right]^2 \right]$, where $\left[\sigma_l^{(R,B)}(k) \right]^2 \triangleq \left[\sigma_l^{(R)}(k) \right]^2 + \left[\sigma_l^{(B)}(k) \right]^2$.

Next, the double difference measurements are obtained. Without loss of generality, the first LEO SV is taken as the reference, yielding the double difference measurements

$$\bar{\mathbf{z}}(k) \triangleq \mathbf{T}\mathbf{z}(k) = \bar{\mathbf{h}}_R(k) + \bar{\mathbf{A}} + \bar{\mathbf{r}}_{\text{leo}}^{(R,B)}(k) + \bar{\mathbf{v}}(k), \quad (5)$$

where $\bar{\mathbf{h}}_R(k) \triangleq \mathbf{T}\mathbf{h}_R(k)$, $\bar{\mathbf{A}} \triangleq \mathbf{T}\mathbf{A}$, $\bar{\mathbf{r}}_{\text{leo}}^{(R,B)}(k) \triangleq \mathbf{T}\tilde{\mathbf{r}}_{\text{leo}}^{(R,B)}(k)$, $\bar{\mathbf{v}}(k) \triangleq \mathbf{T}\mathbf{v}(k)$, and $\mathbf{T} \triangleq [-\mathbf{1}_{L-1} \quad \mathbf{I}_{(L-1) \times (L-1)}]$ is the differencing matrix. Note that the covariance matrix of $\bar{\mathbf{v}}(k)$ is given by $\bar{\mathbf{R}}(k) = \mathbf{T}\mathbf{R}(k)\mathbf{T}^\top$. If λ_l is not equal to λ_1 , then $\bar{\mathbf{A}}$ cannot be expressed as $\lambda\mathbf{N}$, where \mathbf{N} is a vector of integers. If $\lambda_l = \lambda, \forall l$, then $\bar{\mathbf{A}} = \lambda\mathbf{N}$ and the integer ambiguity resolution algorithm described in Subsection II-G is used to resolve the integers.

E. B-WNLS Solution

If the rover remains stationary during the batch window, then the parameter to be estimated is given by

$$\mathbf{x}_{\text{stationary}} \triangleq [\mathbf{r}_{r_R}^\top(0), \bar{\mathbf{A}}^\top]^\top,$$

otherwise, it is given by

$$\mathbf{x}_{\text{mobile}} \triangleq [\mathbf{r}_{r_R}^\top(0), \dots, \mathbf{r}_{r_R}^\top(K-1), \bar{\mathbf{A}}^\top]^\top.$$

The parameter $\mathbf{x}_{\text{stationary}}$ or $\mathbf{x}_{\text{mobile}}$ are estimated from the collection of measurements from 0 to $(K - 1)$ given by

$$\bar{\mathbf{z}}^K \triangleq [\bar{\mathbf{z}}^\top(0), \dots, \bar{\mathbf{z}}^\top(K-1)]^\top,$$

to yield an estimate $\hat{\mathbf{x}}_{\text{stationary}}$ or $\hat{\mathbf{x}}_{\text{mobile}}$, respectively. Let $\hat{\bar{\mathbf{A}}}$ denote the estimate of $\bar{\mathbf{A}}$. For a mobile receiver, the estimation error covariance \mathbf{Q}_A associated with $\hat{\bar{\mathbf{A}}}$ is given by

$$\mathbf{Q}_A = \left(\sum_{k=0}^{K-1} \mathbf{Y}_k^{\frac{1}{2}} \boldsymbol{\Omega}_k \mathbf{Y}_k^{\frac{1}{2}} \right)^{-1},$$

where $\mathbf{Y}_k^{\frac{1}{2}}$ is a square-root of $\mathbf{Y}_k \triangleq \bar{\mathbf{R}}^{-1}(k)$, and

$$\boldsymbol{\Omega}_k \triangleq \mathbf{I}_{(L-1) \times (L-1)} - \boldsymbol{\Psi}_k,$$

$$\boldsymbol{\Psi}_k \triangleq \mathbf{Y}_k^{\frac{1}{2}} \mathbf{T}\mathbf{H}(k) [\mathbf{H}^\top(k)\mathbf{T}^\top \mathbf{Y}_k \mathbf{T}\mathbf{H}(k)]^{-1} \mathbf{H}^\top(k)\mathbf{T}^\top \mathbf{Y}_k^{\frac{1}{2}},$$

where $\mathbf{H}(k)$ is the geometry matrix at time-step k , which can be parameterized by the SVs' azimuth and elevation angles $\{\phi_l\}_{l=1}^L$ and $\{\theta_l\}_{l=1}^L$, respectively, according to

$$\mathbf{H}(k) \triangleq - \begin{bmatrix} \cos[\theta_1(k)]\sin[\phi_1(k)] & \cos[\theta_1(k)]\cos[\phi_1(k)] & \sin[\theta_1(k)] \\ \vdots & \vdots & \vdots \\ \cos[\theta_L(k)]\sin[\phi_L(k)] & \cos[\theta_L(k)]\cos[\phi_L(k)] & \sin[\theta_L(k)] \end{bmatrix}.$$

For a stationary receiver, \mathbf{Q}_N is given by

$$\mathbf{Q}_A = \left[\sum_{k=0}^{K-1} \mathbf{Y}_k - \mathbf{B}_K \mathbf{A}_K^{-1} \mathbf{B}_K^T \right]^{-1},$$

$$\mathbf{A}_K \triangleq \sum_{k=0}^{K-1} \mathbf{H}^T(k) \mathbf{T}^T \mathbf{Y}_k \mathbf{T} \mathbf{H}(k), \quad \mathbf{B}_K \triangleq \sum_{k=0}^{K-1} \mathbf{Y}_k \mathbf{T} \mathbf{H}(k).$$

If $\bar{\mathbf{A}} = \lambda \mathbf{N}$, then an estimate of the integers $\hat{\mathbf{N}}$ and an associated estimation error covariance \mathbf{Q}_N are obtained according to

$$\hat{\mathbf{N}} = \frac{1}{\lambda} \hat{\mathbf{A}}, \quad \mathbf{Q}_N = \frac{1}{\lambda^2} \mathbf{Q}_A.$$

Note that if all measurement noise variances are equal, i.e., $[\sigma_l^{(i)}(k)]^2 = \sigma^2 \forall i, l, k$, then \mathbf{Q}_A and \mathbf{Q}_N may be expressed as

$$\mathbf{Q}_A = \sigma^2 \bar{\mathbf{Q}}_A, \quad \mathbf{Q}_N = \mu^2 \bar{\mathbf{Q}}_A,$$

where $\mu^2 \triangleq \sigma^2 / \lambda^2$ and $\bar{\mathbf{Q}}_A$ is obtained by setting $\mathbf{R}(k) \equiv 2\sigma^2 \mathbf{I}_{L \times L}$.

F. PS-WNLS Solution

After resolving the ambiguities, a point solution for the rover position can be computed at each time-step. Let $\hat{\mathbf{N}}$ denote the integer estimates of \mathbf{N} . The double difference measurement vector adjusted for the integer ambiguities is hence expressed as

$$\bar{\mathbf{z}}_f(k) \triangleq \bar{\mathbf{z}}(k) - \lambda \hat{\mathbf{N}} = \bar{\mathbf{h}}_R(k) + \lambda \tilde{\mathbf{N}} + \bar{\mathbf{r}}_{\text{leo}}^{(R,B)}(k) + \bar{\mathbf{v}}(k),$$

where $\tilde{\mathbf{N}} \triangleq \mathbf{N} - \hat{\mathbf{N}}$ is the integer ambiguity error. The rover uses $\bar{\mathbf{z}}_f(k)$ to solve for $\mathbf{r}_{\text{RR}}(k)$ in a PS-WNLS. For small measurement noise variances, which is the case for high frequency carriers, the positioning performance heavily depends on $\bar{\mathbf{r}}_{\text{leo}}^{(R,B)}(k)$, which is characterized in Section IV.

G. Reduced-Size Integer Least Squares Algorithm

When the proposed LEO constellations are fully deployed, hundreds of LEO satellites will be visible from almost anywhere on Earth. As an example, Fig. 3 shows a heat map of the number of visible Starlink LEO SVs for an elevation mask of 5° . Dozens of satellites will still be visible for even higher elevation masks. For example, 60 Starlink LEO SVs will be visible over Irvine, CA, U.S.A. for a 25° elevation mask. For such number of satellites, it is impractical to solve the ILS, as its complexity grows exponentially with the number of integer ambiguities [35]. This subsection proposes an integer ambiguity resolution algorithm, referred to as reduced-size ILS, which approaches the performance of the Least-squares AMbiguity

Decorrelation Adjustment (LAMBDA) method [35], but with a significantly smaller fraction of the LAMBDA method's complexity. The reduced-size ILS relies on the tradeoff between complexity and performance. That is, for every integer, a test is formulated to determine whether the Integer Rounding (IR) method, which has negligible complexity, is a good estimate of the corresponding integer, or whether the integer must be estimated using an ILS.

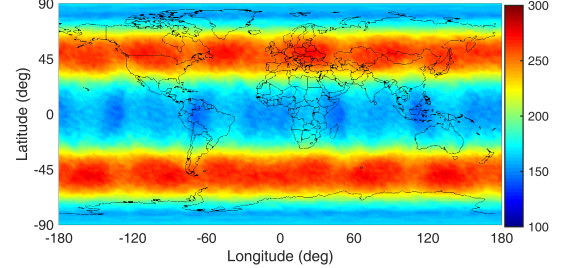


Fig. 3. Heat map of the number of visible Starlink LEO satellites at any point on Earth for an elevation mask of 5° .

The test is of the form

$$[\bar{\mathbf{Q}}_N]_{ll} \stackrel{?}{\leq} \frac{1}{\mu^2} \eta, \quad (6)$$

where $[\bar{\mathbf{Q}}_N]_{ll}$ is the l -th diagonal element of $\bar{\mathbf{Q}}_N$ after decorrelation. The choice of η is discussed in Subsection IV-B. An integer estimated by IR is said to be reliable if it satisfies (6). Next, define the set of reliable integers \mathcal{S}_R as

$$\mathcal{S}_R = \left\{ l \mid [\bar{\mathbf{Q}}_N]_{ll} \leq \frac{1}{\mu^2} \eta \right\}. \quad (7)$$

The complimentary set is denoted by $\bar{\mathcal{S}}_R$. The next step of the algorithm is reducing the size and performing the ILS on the reduced set $\bar{\mathcal{S}}_R$. To this end, the vector $\hat{\mathbf{N}}$ and its corresponding covariance matrix are rearranged as

$$\hat{\mathbf{N}}_P = \begin{bmatrix} \hat{\mathbf{N}}_{\mathcal{S}_R}^T & \hat{\mathbf{N}}_{\bar{\mathcal{S}}_R}^T \end{bmatrix}^T, \quad \mathbf{Q}_{NP} = \begin{bmatrix} \mathbf{Q}_{\mathcal{S}_R} & \mathbf{Q}_{\mathcal{S}_R \bar{\mathcal{S}}_R} \\ \mathbf{Q}_{\bar{\mathcal{S}}_R \mathcal{S}_R} & \mathbf{Q}_{\bar{\mathcal{S}}_R} \end{bmatrix}, \quad (8)$$

where each element of $\hat{\mathbf{N}}_{\mathcal{S}_R}$ belongs to the set $\left\{ [\hat{\mathbf{N}}]_l \mid l \in \mathcal{S}_R \right\}$. Let $\tilde{\mathbf{N}}_R$ denote the IR solution of $\hat{\mathbf{N}}_{\mathcal{S}_R}$. Subsequently, the original ILS problem may be reduced as

$$\tilde{\mathbf{N}}_{\text{eff}} = \arg \min_{\mathbf{N}_{\text{eff}} \in \mathbb{Z}^{L_{\text{eff}}}} \|\hat{\mathbf{N}}_{\text{eff}} - \mathbf{N}_{\text{eff}}\|_{\mathbf{Q}_{\mathcal{S}_R}}^2, \quad (9)$$

where $\hat{\mathbf{N}}_{\text{eff}} \in \mathbb{R}^{L_{\text{eff}}}$ is the "effective" real-valued estimate of the remaining integers to be resolved using the ILS, and is computed using the minimum mean square error (MMSE) estimate given by

$$\hat{\mathbf{N}}_{\text{eff}} = \hat{\mathbf{N}}_{\bar{\mathcal{S}}_R} + \mathbf{Q}_{\bar{\mathcal{S}}_R \mathcal{S}_R} \mathbf{Q}_{\mathcal{S}_R}^{-1} \left(\hat{\mathbf{N}}_{\mathcal{S}_R} - \tilde{\mathbf{N}}_R \right). \quad (10)$$

Let $\tilde{\mathbf{N}}$ denote the final integer estimate, which combines the reliable IR estimates and the estimates obtained from the reduced ILS. It is shown in Subsection IV-B that L_{eff} may approach zero at some regimes of μ^2 . This implies that the proposed method achieves the LAMBDA method's performance without any ILS search for many practical realizations of \mathbf{Q}_N .

III. DERIVATION OF THE JOINT DISTRIBUTION OF MEGACONSTELLATION LEO SVs' AZIMUTH AND ELEVATION ANGLES

In this section, the joint pdf of megaconstellation LEO SVs' azimuth and elevation angles is derived. This pdf offers an efficient way to characterize the performance of the CD-LEO framework as well as to enable performance-driven design of the CD-LEO framework, such as the differential baseline and the B-WNLS batch window. The orbit of a LEO SV is defined by its inclination angle i_l and orbital altitude h_l . Define the normalized orbital radius

$$\alpha_l \triangleq 1 + \frac{h_l}{R_E}, \quad (11)$$

where R_E is the average radius of the Earth, which is assumed to be spherical. The SV's position will be uniformly distributed over its orbital plane. The surface over which the LEO SV can exist is defined as $\mathbb{B}_o(i_l, R_{h_l})$, which is a capless sphere of radius $R_{h_l} \triangleq \alpha_l R_E$, as shown in Fig. 4. Let ϕ_l and θ_l denote the azimuth and elevation angles, respectively, of the l -th LEO SV. These angles are specific to a receiver location given by longitude λ_0 and latitude φ_0 . Moreover, let $\gamma(\theta_l)$ denote the angle between the LEO SV and receiver position vectors. Using the law of sines, $\gamma(\theta_l)$ can be expressed as

$$\gamma(\theta_l) = \cos^{-1} \left[\frac{1}{\alpha_l} \cos \theta_l \right] - \theta_l. \quad (12)$$

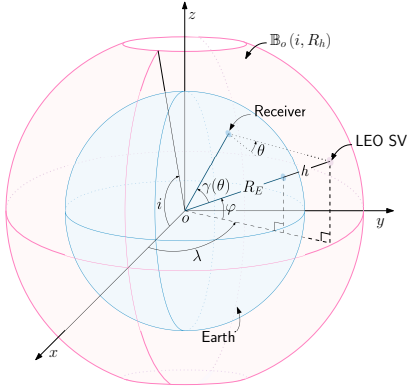


Fig. 4. LEO SV-to-receiver geometry. The subscript l is omitted for simplicity.

A. Stationarity of Elevation and Azimuth Angle Distribution

It is important to establish the stationarity of the azimuth and elevation angle distribution. The analysis in Section IV assumes that the elevation angle are stationary and uncorrelated in time. This assumption becomes valid for megaconstellations where the distribution does remain close to stationary. To illustrate this, the Starlink LEO SV constellation is shown in Fig. 5(a). The constellation parameters are obtained from the proposed Starlink constellation in [39] and are summarized in Table I. Fig. 5(b) shows an SV orbit with orbital radius αR_E and phase ν between SVs. If CD-LEO measurements are taken at intervals T_ν , where T_ν is the time needed for an SV to cross the phase ν , then the SV distribution will seem stationary to the receiver. In the case of the Starlink constellation, $T_\nu \approx 128$ seconds, and will be even smaller

for their future very LEO (VLEO) constellation ($T_\nu \approx 68$ seconds). This time will become even smaller when all the LEO constellations are combined in the analysis. In the sequel, it is assumed that the elevation and azimuth angles are sampled at the sampling interval $T > T_\nu$.

TABLE I
STARLINK ORBITAL CONFIGURATION

Parameter	LEO constellation				
Satellites per altitude	1600	1600	400	375	450
Altitude (km)	1150	1110	1130	1275	1325
Inclination ($^\circ$)	53	53.8	74	81	70

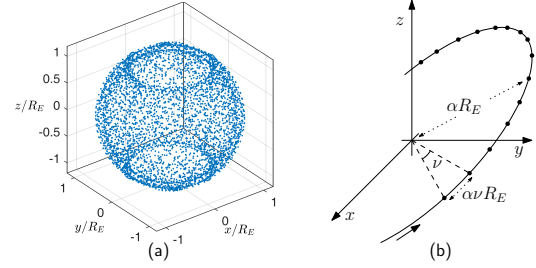


Fig. 5. (a) Starlink constellation obtained from the parameters in Table I. The SV coordinates were normalized by the average Earth radius R_E . (b) SV orbit showing the phase ν between successive SVs.

B. Satellite Longitude and Latitude Distribution Model

Given an SV's longitude λ_l measured from the ascending node, it can be shown that the SV's latitude φ_l is given by

$$\varphi_l = \sin^{-1} [\sin i_l \cdot \sin \lambda_l]. \quad (13)$$

By design, λ_l is uniformly distributed over the $[0, 2\pi)$ interval.

Subsequently, using random variable transformation, the pdfs of λ_l and φ_l are given by

$$f_\Lambda(\lambda_l) = \begin{cases} \frac{1}{2\pi}, & 0 \leq \lambda_l < 2\pi \\ 0, & \text{elsewhere,} \end{cases} \quad (14)$$

$$f_\Psi(\varphi_l) = \begin{cases} \frac{\cos \varphi_l}{\pi \sqrt{\sin^2 i_l - \sin^2 \varphi_l}}, & |\varphi_l| < i_l \\ 0, & \text{elsewhere,} \end{cases} \quad (15)$$

with the joint pdf given by

$$f_{\Lambda, \Psi}(\lambda_l, \varphi_l) = f_\Lambda(\lambda_l) f_\Psi(\varphi_l). \quad (16)$$

The histogram obtained from the Starlink constellation and the analytical pdfs for $i_l = 53^\circ$ are shown in Fig. 6.

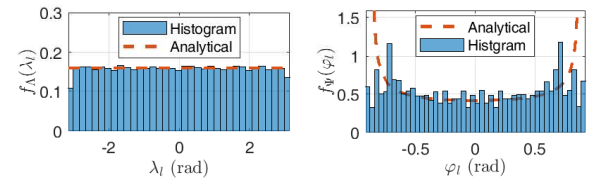


Fig. 6. Histogram and analytical pdfs of λ_l and φ_l for $i_l = 53^\circ$.

C. Satellite Elevation and Azimuth Distribution Model

The joint pdf of ϕ_l and θ_l , denoted by $f_{\Phi, \Theta}(\phi_l, \theta_l)$, can be obtained from $f_{\Lambda, \Psi}(\lambda_l, \varphi_l)$ through coordinate transformation. To this end, the mapping from the pair (ϕ_l, θ_l) to (λ_l, φ_l) must be established. The result is captured in the following lemma.

Lemma III.1. Given a spherical Earth, an SV orbit characterized by i_l and α_l , and a receiver's longitude λ_0 and latitude φ_0 , the inverse mapping from (ϕ_l, θ_l) to (λ_l, φ_l) is given by

$$\mathbf{y}(\phi_l, \theta_l) \triangleq \begin{bmatrix} \lambda_l \\ \varphi_l \end{bmatrix} = \begin{bmatrix} \tan^{-1} \left[\frac{a_{02}(\phi_l, \theta_l)}{a_{01}(\phi_l, \theta_l)} \right] \\ \sin^{-1} [a_{03}(\phi_l, \theta_l)] \end{bmatrix}, \quad (17)$$

where

$$\begin{aligned} a_{01}(\phi_l, \theta_l) &\triangleq \sin[\gamma(\theta_l)] f_{01}(\phi_l, \theta_l) + \frac{1}{\alpha_l} \cos \varphi_0 \cos \lambda_0 \\ a_{02}(\phi_l, \theta_l) &\triangleq \sin[\gamma(\theta_l)] f_{02}(\phi_l, \theta_l) + \frac{1}{\alpha_l} \cos \varphi_0 \sin \lambda_0 \\ a_{03}(\phi_l, \theta_l) &\triangleq \sin[\gamma(\theta_l)] f_{03}(\phi_l, \theta_l) + \frac{1}{\alpha_l} \sin \varphi_0, \end{aligned}$$

$$\begin{aligned} f_{01}(\phi, \theta) &\triangleq \cos \varphi_0 \cos \lambda_0 \tan \theta - \sin \lambda_0 \sin \phi - \sin \varphi_0 \cos \lambda_0 \cos \phi \\ f_{02}(\phi, \theta) &\triangleq \cos \varphi_0 \sin \lambda_0 \tan \theta + \cos \lambda_0 \sin \phi - \sin \varphi_0 \sin \lambda_0 \cos \phi \\ f_{03}(\phi, \theta) &\triangleq \sin \varphi_0 \tan \theta + \cos \varphi_0 \cos \phi. \end{aligned}$$

Proof. For a spherical Earth, the l -th satellite position in Earth-centered Earth-fixed (ECEF) may be expressed as

$$\bar{\mathbf{r}}_{\text{leo}_l} = \alpha_l R_E [\cos \varphi_l \cos \lambda_l, \cos \varphi_l \sin \lambda_l, \sin \varphi_l]^\top.$$

Subsequently, given $\bar{\mathbf{r}}_{\text{leo}_l}$, the longitude and latitude λ_l and φ_l , respectively, may be obtained according to

$$\lambda_l = \tan^{-1} \left[\frac{\mathbf{e}_2^\top \bar{\mathbf{r}}_{\text{leo}_l}}{\mathbf{e}_1^\top \bar{\mathbf{r}}_{\text{leo}_l}} \right], \quad \varphi_l = \sin^{-1} \left[\frac{\mathbf{e}_3^\top \bar{\mathbf{r}}_{\text{leo}_l}}{\|\bar{\mathbf{r}}_{\text{leo}_l}\|_2} \right]. \quad (18)$$

The SV position in ENU can also be expressed as

$$\mathbf{r}_{\text{leo}_l} \triangleq d_l [\cos \theta_l \sin \phi_l, \cos \theta_l \cos \phi_l, \sin \theta_l]^\top, \quad (19)$$

where d_l is the distance between the SV and the receiver. Using the law of sines, d_l may be expressed as

$$d_l = \alpha_l R_E \frac{\sin[\gamma(\theta_l)]}{\cos \theta_l}. \quad (20)$$

Using coordinate frame transformation, the SV position in ECEF can be obtained from \mathbf{r}_{leo} through

$$\bar{\mathbf{r}}_{\text{leo}_l} = \mathbf{R}^\top(\varphi_0, \lambda_0) \mathbf{r}_{\text{leo}_l} + \bar{\mathbf{r}}_{r_i}, \quad (21)$$

where $\bar{\mathbf{r}}_{r_i} = R_E [\cos \varphi_0 \cos \lambda_0, \cos \varphi_0 \sin \lambda_0, \sin \varphi_0]^\top$ is the receiver's position in ECEF and $\mathbf{R}(\varphi_0, \lambda_0)$ is the ECEF to ENU rotation matrix with

$$\mathbf{R}(\varphi_0, \lambda_0) \triangleq \begin{bmatrix} -\sin \lambda_0 & \cos \lambda_0 & 0 \\ -\sin \varphi_0 \cos \lambda_0 & -\sin \varphi_0 \sin \lambda_0 & \cos \varphi_0 \\ \cos \varphi_0 \cos \lambda_0 & \cos \varphi_0 \sin \lambda_0 & \sin \varphi_0 \end{bmatrix}.$$

Equation (17) is readily obtained by combining (18)–(21). \square

Finally, $f_{\Phi, \Theta}(\phi_l, \theta_l)$ is given by

$$f_{\Phi, \Theta}(\phi_l, \theta_l) = \begin{cases} \frac{|\det[\mathbf{J}_y(\phi_l, \theta_l)]| \sqrt{1 - a_{03}^2(\phi_l, \theta_l)}}{2\pi^2 \sqrt{\sin^2 i_l - a_{03}^2(\phi_l, \theta_l)}}, & |a_{03}(\phi_l, \theta_l)| < \sin i_l \\ 0, & \text{elsewhere,} \end{cases} \quad (22)$$

where $\mathbf{J}_y(\phi_l, \theta_l) \triangleq \begin{bmatrix} \frac{\partial \lambda_l}{\partial \phi_l} & \frac{\partial \lambda_l}{\partial \theta_l} \\ \frac{\partial \varphi_l}{\partial \phi_l} & \frac{\partial \varphi_l}{\partial \theta_l} \end{bmatrix}$. The expression of $\mathbf{J}_y(\phi_l, \theta_l)$ and its determinant are given in Appendix A.

D. Azimuth and Elevation Joint Distribution for a Set Elevation Mask

Since the visible SVs have non-negative elevation angles, one is interested to know the pdf for $\theta_l \geq 0$. In practice, a positive elevation mask θ_{\min} is set. The pdf for $\theta_l \geq \theta_{\min}$ is hence given by

$$f_{\Phi, \Theta}^{\theta_{\min}}(\phi_l, \theta_l) = \begin{cases} \frac{|\det[\mathbf{J}_y(\phi_l, \theta_l)]| \sqrt{1 - a_{03}^2(\phi_l, \theta_l)}}{C_{i_l, \theta_{\min}} \sqrt{\sin^2 i_l - a_{03}^2(\phi_l, \theta_l)}}, & (\phi_l, \theta_l) \in \mathcal{D}_{i_l, \theta_{\min}} \\ 0, & \text{elsewhere,} \end{cases} \quad (23)$$

where the domain $\mathcal{D}_{i_l, \theta_{\min}}$ is defined as

$$\mathcal{D}_{i_l, \theta_{\min}} = [(\phi_l, \theta_l) \mid (|a_{03}(\phi_l, \theta_l)| < \sin i_l) \cap (\theta_l \geq \theta_{\min})],$$

and the normalization constant $C_{i_l, \theta_{\min}}$ is given by

$$C_{i_l, \theta_{\min}} = 2\pi^2 \int \int_{\mathcal{D}_{i_l, \theta_{\min}}} f_{\Phi, \Theta}(\phi_l, \theta_l) d\phi_l d\theta_l.$$

Note that one can find the average number of visible satellites \bar{L} according to

$$\bar{L} = L \times \Pr[\theta_l \geq \theta_{\min}] = L \frac{C_{i_l, \theta_{\min}}}{2\pi^2}, \quad (24)$$

where L is the total number of SVs in the constellation.

E. Multi-constellation Azimuth and Elevation Joint Distribution

Recall that the pdf in (23) is constellation-specific, i.e., it is parameterized by one inclination angle i_l and one normalized orbital radius α_l . For the case of multi-constellations, as is the case for LEO megaconstellation, the joint pdf for all constellations, each of which defined by is given by

$$\text{all } f_{\Phi, \Theta}^{\theta_{\min}}(\phi_l, \theta_l) = \sum_{j=1}^J p_j^j f_{\Phi, \Theta}^{\theta_{\min}}(\phi_l, \theta_l), \quad (25)$$

where J is the total number of constellations, L_j is the number of satellites in the j -th constellation, $f_{\Phi, \Theta}^{\theta_{\min}}(\phi_l, \theta_l)$ is the pdf of the j -th constellation obtained according to (23), and $p_j \triangleq \frac{L_j}{\sum_{j=1}^J L_j}$ is the probability of a particular SV being part of the j -th constellation.

IV. PERFORMANCE CHARACTERIZATION AND PERFORMANCE-DRIVEN CD-LEO FRAMEWORK DESIGN

This section studies the PDOP, shows a methodology to obtain the optimal threshold for the proposed reduced-ILS method, and characterizes the measurement error in the PS-WNLS due to satellite position errors.

A. PDOP Characterization

One important measure of the estimability (i.e., degree of observability) of the receiver's position is the PDOP. Assuming equal measurement noise variances, the PDOP in the CD-LEO framework is given by $\text{PDOP} = \text{trace}[\mathbf{P}]$, where \mathbf{P} is the PDOP matrix given by

$$\mathbf{P} = 2 \left[\mathbf{H}^\top \mathbf{T}^\top (\mathbf{T} \mathbf{T}^\top)^{-1} \mathbf{T} \mathbf{H} \right]^{-1}.$$

Another metric of interest is the horizontal dilution of precision (HDOP), which gives a measure of the estimability of the horizontal components of the position vector. This metric is appropriate to study in the case where the rover is equipped with an altimeter and is using LEO signals mainly to estimate its horizontal position. The HDOP is calculated according to $\text{PDOP} = \text{trace}[\mathbf{P}_{2 \times 2}]$, where $\mathbf{P}_{2 \times 2}$ indicates the 2×2 block of the PDOP matrix corresponding to the horizontal position coordinates. The PDOP and HDOP cumulative density functions (cdfs) are characterized numerically using the pdfs of the SV azimuth and elevation angles derived in Section III for the Starlink constellation with the parameters in Table I. The cdfs, shown in Fig. 7 are computed for a receiver in Irvine, CA, U.S.A., and for three elevation angle masks: 5° , 25° , and 35° . Fig. 7 shows that the PDOP is mostly less than 2 for elevation angle masks of 25° or below, and above 2 almost all the time for elevation angle masks of 35° . This is mainly due to the fact that the vertical component becomes poorly observable for such elevation angle masks. This is validated in the HDOP cdf, which shows that the HDOP is almost always below unity for elevation masks of 35° or below. In fact, the HDOP is mostly below 0.6 for elevation angles of 25° , showing that highly accurate horizontal positioning may be achieved.

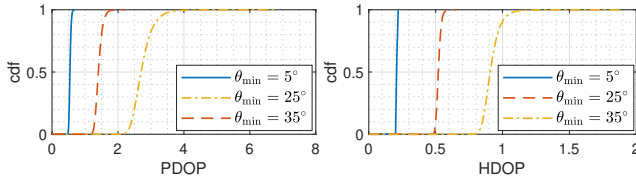


Fig. 7. Cdf of the PDOP and HDOP in the CD-LEO framework for the Starlink constellation.

B. Reduced-Size ILS Threshold Selection

The optimal threshold η for the integer ambiguity resolution algorithm presented in Subsection II-G was characterized numerically for the Starlink constellation with the parameters shown in Table I. The receiver was assumed stationary and was located on the UCI campus. Several realizations of SV elevation and azimuth angles were generated for different values of σ^2 , and the threshold $\eta(\sigma^2)$ was selected as the minimum threshold that maximizes the success rate of the proposed method. The elevation mask was set to 35° .

Fig. 8(a) demonstrates the success rate, i.e., $\Pr[\tilde{\mathbf{N}} = \mathbf{N}]$ [40], for (i) the method proposed in Subsection II-G using the numerically computed threshold, (ii) the IR method, and (iii) the LAMBDA method for $\theta_{\min} = 35^\circ$, $L = 25$, and $K = 7$. It can be observed that the performance of the proposed method approaches that of the LAMBDA method as μ^2 decreases. Fig. 8(b) shows the average size of \mathbf{N}_{eff} denoted by L_{eff} , which is the dimension of the unknown integer vector in the proposed reduced-size ILS algorithm. It can be seen that L_{eff} is at most 32% that of the size of the original ILS problem, reducing the complexity of the ILS search by orders of magnitude.

C. Measurement Errors Due to Ephemeris Errors

Recall that the SV positions are obtained by non-precise ephemerides. The effect of the estimated SV position error

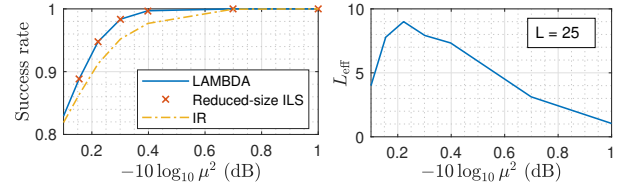


Fig. 8. (a) Success rates of (i) the LAMBDA method, (ii) IR, (iii) and the proposed reduced-size ILS method with the numerically computed threshold. (b) The effective number of integers to solve for in the reduced-size ILS.

onto the CD-LEO measurement is first characterized as a function of the SV elevation angle. Next, the pdf of the elevation angle derived in III is used to obtain the cdf of the measurement error due to ephemeris errors. A first-order Taylor series expansion around $\hat{\mathbf{r}}_{\text{leol}}$ yields

$$\|\mathbf{r}_{r_i} - \mathbf{r}_{\text{leol}}\|_2 \approx \|\mathbf{r}_{r_i} - \hat{\mathbf{r}}_{\text{leol}}\|_2 + \mathbf{h}_{i_l}^T \tilde{\mathbf{r}}_{\text{leol}},$$

where \mathbf{h}_{i_l} is the unit line-of-sight vector between the l -th LEO SV and the i -th receiver. A first-order Taylor series expansion around \mathbf{h}_{B_l} yields

$$\mathbf{h}_{R_l} \approx \mathbf{h}_{B_l} + \frac{1}{\|\mathbf{r}_{r_B} - \hat{\mathbf{r}}_{\text{leol}}\|_2} (\mathbf{I} - \mathbf{h}_{B_l} \mathbf{h}_{B_l}^T) \Delta \mathbf{r}_b,$$

where $\Delta \mathbf{r}_b$ is the baseline vector between the base and the rover. Subsequently, the residual due to SV position errors can be expressed as

$$\begin{aligned} \tilde{\mathbf{r}}_{\text{leol}}^{(R,B)} &= \|\mathbf{r}_{r_R} - \mathbf{r}_{\text{leol}}\|_2 - \|\mathbf{r}_{r_B} - \mathbf{r}_{\text{leol}}\|_2 \\ &\quad - \|\mathbf{r}_{r_R} - \hat{\mathbf{r}}_{\text{leol}}\|_2 + \|\mathbf{r}_{r_B} - \hat{\mathbf{r}}_{\text{leol}}\|_2 \\ \Rightarrow \tilde{\mathbf{r}}_{\text{leol}}^{(R,B)} &\approx \frac{(\mathbf{\Xi}_l \tilde{\mathbf{r}}_{\text{leol}})^T (\mathbf{\Xi}_l \Delta \mathbf{r}_b)}{\|\mathbf{r}_{r_B} - \hat{\mathbf{r}}_{\text{leol}}\|_2}, \end{aligned}$$

where $\mathbf{\Xi}_l \triangleq (\mathbf{I} - \mathbf{h}_{B_l} \mathbf{h}_{B_l}^T)$. The residual can be interpreted as the dot product between the baseline projected onto the range-space of $\mathbf{\Xi}_l$, denoted $\mathcal{R}(\mathbf{\Xi}_l)$, and the SV position error vector also projected onto $\mathcal{R}(\mathbf{\Xi}_l)$, as shown in Fig. 9.

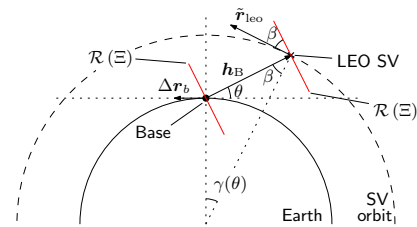


Fig. 9. Baseline-to-SV geometry. The subscript l was omitted for simplicity. The red lines show the range-space of $\mathbf{\Xi}$, denoted by $\mathcal{R}(\mathbf{\Xi})$, which is orthogonal to the unit line-of-sight vector \mathbf{h}_B .

It can be seen from Fig. 9 that the magnitude of $\tilde{\mathbf{r}}_{\text{leol}}^{(R,B)}$ is maximized when the SV's ground track is collinear with the baseline. In such cases, using (20), the magnitude of $\tilde{\mathbf{r}}_{\text{leol}}^{(R,B)}$ may be bounded according to

$$\left| \tilde{\mathbf{r}}_{\text{leol}}^{(R,B)} \right| \leq \left| g(\theta_l^{(B)}, \alpha_l) \right| \frac{\|\Delta \mathbf{r}_b\|_2 \|\tilde{\mathbf{r}}_{\text{leol}}\|_2}{R_E}, \quad (26)$$

where

$$g(\theta, \alpha) = \frac{\sin \theta \cos \theta \sqrt{\alpha^2 - \cos^2 \theta}}{\alpha^2 \sin \left[\cos^{-1} \left(\frac{\cos \theta}{\alpha} \right) - \theta \right]}.$$

Subsequently, the cdf of $|\tilde{r}_{\text{leo}_r}^{(R,B)}|$ can be characterized from (26) and the joint distribution of the LEO SVs' azimuth and elevation angles derived in Section III. To this end, the cdf of $g(\theta, \alpha)$ is calculated for the Starlink LEO constellation using the parameters in Table I. The receiver was assumed to be on the UCI campus. The cdf was computed for three elevation masks: $\theta_{\min} = 5^\circ$, $\theta_{\min} = 25^\circ$, and $\theta_{\min} = 35^\circ$. The cdf of $g(\theta, \alpha)$ is shown in Fig. 10(a), and the expected value of $g(\theta, \alpha)$, denoted by $\mathbb{E}[g(\theta, \alpha)]$ is shown in Fig. 10(b) as a function of θ_{\min} .

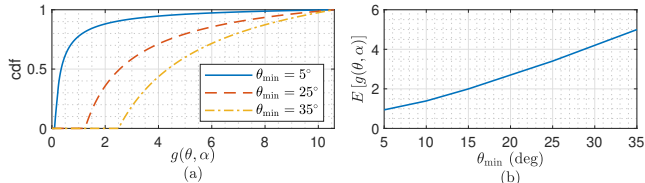


Fig. 10. (a) Cdf of $g(\theta, \alpha)$ for $\theta_{\min} = 5^\circ$, $\theta_{\min} = 25^\circ$, and $\theta_{\min} = 35^\circ$. (b) Expected value of $g(\theta, \alpha)$ as a function of θ_{\min} .

V. EXPERIMENTAL RESULTS

This section presents experimental results of a UAV navigating with signals from Orbcomm LEO SVs via the CD-LEO framework discussed in Section II. First, the experimental setup is discussed. Then, the navigation frameworks implemented in the experiments and their associated results are presented.

A. Experimental Setup

To demonstrate the CD-LEO framework discussed in Section II, the rover was a DJI Matrice 600 UAV equipped with an Ettus E312 USRP, a high-end VHF antenna, and a small consumer-grade GPS antenna to discipline the on-board oscillator. The base was a stationary receiver equipped with an Ettus E312 USRP, a custom-made VHF antenna, and a small consumer-grade GPS antenna to discipline the on-board oscillator. The receivers were tuned to a 137 MHz carrier frequency with 2.4 MHz sampling bandwidth, which covers the 137–138 MHz band allocated to Orbcomm SVs. Samples of the received signals were stored for off-line post-processing using the software-defined radio (SDR) developed in [8]. The LEO carrier phase measurements were produced at a rate of 4.8 kHz and were downsampled to 10 Hz. The base's position was surveyed on Google Earth, and the UAV trajectory was taken from its on-board navigation system, which uses GNSS (GPS and GLONASS), an inertial measurement unit (IMU), and other sensors. The hovering horizontal precision of the UAV is reported to be 1.5 meters by DJI. The experimental setup is shown in Fig. 11. The UAV traversed a total trajectory of 2.28 km in 120 seconds.

Over the course of the experiment, the receivers on-board the base and the UAV were listening to 2 Orbcomm SVs, namely FM 108 and FM 116. The SVs transmit their position as estimated by their on-board GPS receivers. These positions were decoded and used as ground-truth. A position estimate of FM 108 and FM 116 was also obtained from TLE files and

SGP4 software [41]. The satellites were simultaneously visible for 2 minutes. A sky plot of the 2 Orbcomm SVs is shown in Fig. 12(a). The Doppler frequency measured by the rover using the SDR in [8] for the 2 Orbcomm SVs is shown along the expected Doppler calculated from the TLE files in Fig. 12(b). The SV position error and the range residuals were shown in Fig. 1 for each SV. Fig. 13(a) shows the SV trajectories.

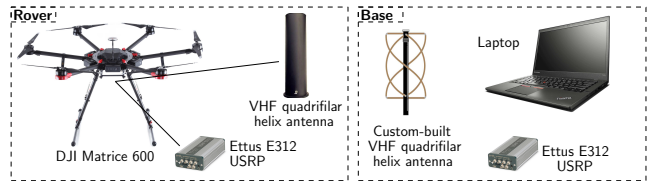


Fig. 11. Base/rover experimental setup of the CD-LEO framework.

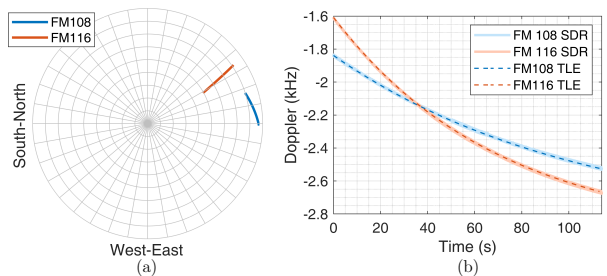


Fig. 12. (a) Sky plot of the geometry of the 2 Orbcomm SVs during the experiment. (b) The measured Doppler frequencies using the proprietary SDR and the expected Doppler calculated from the TLE for both Orbcomm SVs.

Since only 2 satellites were visible at a time, which is the case with many of the current LEO constellations, an extended Kalman filter (EKF) was used to estimate the three-dimensional (3-D) position and velocity of the UAV from single difference measurements. To demonstrate the potential of the CD-LEO navigation framework, two frameworks were implemented for comparison: (i) a modified version of the CD-LEO framework discussed in Section II and (ii) a non-differential framework that employs carrier phase LEO measurements from the UAV's receiver only. The results of each framework are presented next.

B. CD-LEO Framework Experimental Results

Single difference measurements provide more information on the SV-to-receiver geometry than double difference measurements since the differencing matrix \mathbf{T} is not applied [42]. This comes at the cost of an additional state to be estimated: the common clock bias $\delta t_r^{(R,B)}(k)$. To this end, the UAV's position and velocity states were estimated along with the common clock bias $\delta t_r^{(R,B)}(k)$ and the constant ambiguity $N_2^{(R,B)}$. Note that $N_1^{(R,B)}$ was lumped into $\delta t_r^{(R,B)}(k)$. The UAV's position and velocity were assumed to evolve according to a nearly constant velocity model, and the common clock state was assumed to evolve according to the standard model of double integrator driven by noise as discussed in [43], [44]. A prior for the UAV position and velocity was obtained from the UAV's on-board system. The prior was used to initialize the EKF. After initialization, the EKF was using single-difference Orbcomm LEO SV measurements to estimate the states of the

UAV. To study the effect of ephemeris errors on the navigation solution, two EKF s were implemented: (i) one that uses the Orbcmm LEO SV positions estimated by the SVs' on-board GPS receiver and (ii) one that uses the Orbcmm LEO SV positions estimated from TLE files. The estimated trajectories are shown in Fig. 13(b) and Fig. 13(c). The EKF position estimation errors are shown in Fig. 14 along with the 3σ bounds. Note that since the UAV mainly travels in the North direction, the East direction becomes poorly estimable; hence, the 3σ bounds in the East direction increase at a higher rate than the 3σ bound in the North direction, as shown in Fig. 14. The common clock bias estimate and the corresponding $\pm 3\sigma$ bounds are also shown in Fig 14. The 3-D position root mean squared errors (RMSEs) and final errors for both EKF s are shown in Table II.

C. Non-Differential LEO Framework Experimental Results

To demonstrate the importance of the CD-LEO framework, a non-differential LEO framework is implemented. To this end, the UAV's position and velocity are estimated in an EKF using the non-differential measurements in (1). In this case, two clock biases must be estimated capturing the difference between the receiver's clock bias and each of the Orbcmm LEO SVs' bias. The same dynamics models and initialization method employed in Subsection V-B were used in the non-differential framework. Similarly to Subsection V-B, two EKF s were implemented: (i) one that uses the Orbcmm LEO SV positions estimated by the SVs' on-board GPS receiver and (ii) one that uses the Orbcmm LEO SV positions estimated from TLE files. The estimated trajectories are shown in Fig. 13(b) and Fig. 13(c). The EKF position estimation errors are shown in Fig. 15 along with the associated 3σ bounds. The clock bias estimate associated with FM 108 and the corresponding $\pm 3\sigma$ bounds are also shown in Fig 14. The 3-D position RMSEs and final errors for both EKF s are shown in Table II.

D. Discussion

Table II summarizes the experimental results for the CD-LEO and non-differential LEO frameworks. It can be seen from Fig. 1 that the residuals in the non-differential carrier phase measurements are on the order of kilometers, which explains the unacceptably large RMSEs of the non-differential framework. While using the SV positions transmitted by the Orbcmm SVs reduces the RMSEs, the errors remain unacceptably large in the non-differential framework due to other unmodeled errors. Such errors cancel out in the CD-LEO framework, yielding acceptable performance whether SV positions from GPS or TLE are used. The accuracy of these results is *unprecedented*, considering that (i) only 2 LEO SVs were used, (ii) no other sensors were fused into the navigation, and (iii) these LEO SVs are not intended for navigation and are exploited opportunistically. The double difference residual due to ephemeris errors was calculated, and is shown in Fig. 16. During the experiment, the baseline varied between 20 m and 200 m. According to Subsection II-A, the function $g(\theta, \alpha)$ averages to 1.346 for the Orbcmm constellation, which has

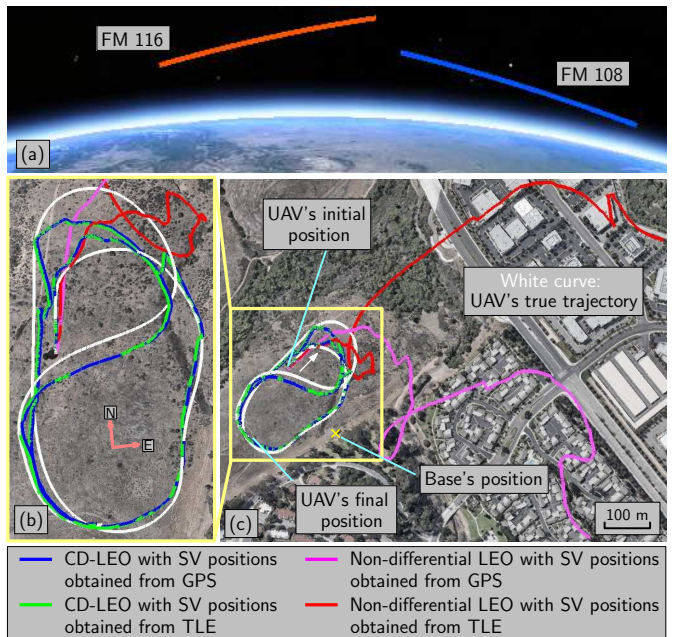


Fig. 13. (a) Trajectories of the 2 Orbcmm LEO SVs. (b)–(c) True and estimated trajectories of the UAV. Map data: Google Earth.

an inclination angle of 45° and orbital altitude of 800 km and $\theta_{\min} = 5^\circ$. From the SV position errors in Fig. 1, the expected range of the residuals is from 0.3 to 16 cm. It can be seen from Fig. 16 that the magnitude of the double difference residual is on the order of *centimeters* and matches the expected values, showing (i) the robustness of the CD-LEO framework against ephemeris errors and (ii) the accuracy of the performance analysis framework discussed in Section IV.

TABLE II
EXPERIMENTAL RESULTS RMSEs AND FINAL ERRORS

Framework	SV position source	RMSE	Final error
CD-LEO	GPS	14.8 m	3.9 m
CD-LEO	TLE	15.0 m	4.8 m
Non-differential	GPS	338.6 m	590.4 m
Non-differential	TLE	405.4 m	759.5 m

VI. CONCLUSION

This paper proposed a differential framework for opportunistic navigation with carrier phase measurements from megaconstellation LEO satellites. A computationally efficient integer ambiguity resolution algorithm was proposed to reduce the size of the ILS problem, with simulation using the Starlink constellation as a specific megaconstellation example showing a 60% reduction in the size of the ILS problem while maintaining optimality. Moreover, the joint pdf of the megaconstellation LEO satellites' azimuth and elevation angle was derived. A performance characterization of the proposed CD-LEO framework was conducted using derived joint azimuth and elevation angle pdf, showing the potential of LEO satellite signals for precise navigation. The performance characterization conducted herein also facilitates system parameter design to meet desired performance requirements. Experimental results were presented showing a UAV navigating for 2.28 km exclusively using signals from only two Orbcmm LEO SVs

via the proposed framework with an unprecedented position RMSE of 14.8 m over a period of 2 minutes.

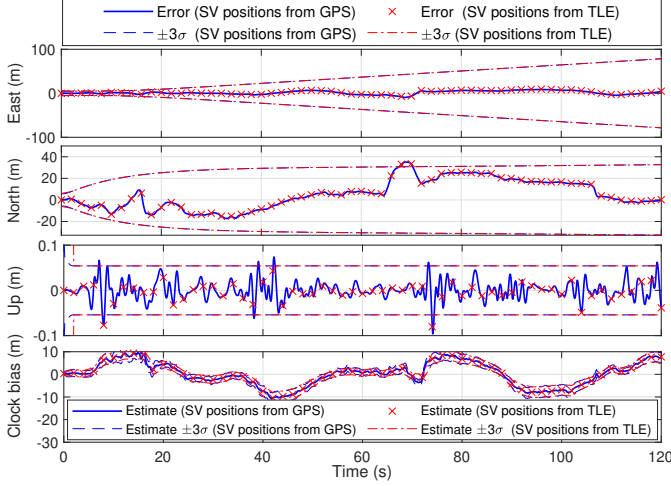


Fig. 14. EKF position estimation error and $\pm 3\sigma$ bounds for the CD-LEO framework. The estimates and sigma bounds for the case where SV positions are obtained from GPS and the ones for the case where the SV positions are obtained from TLE files are almost identical.

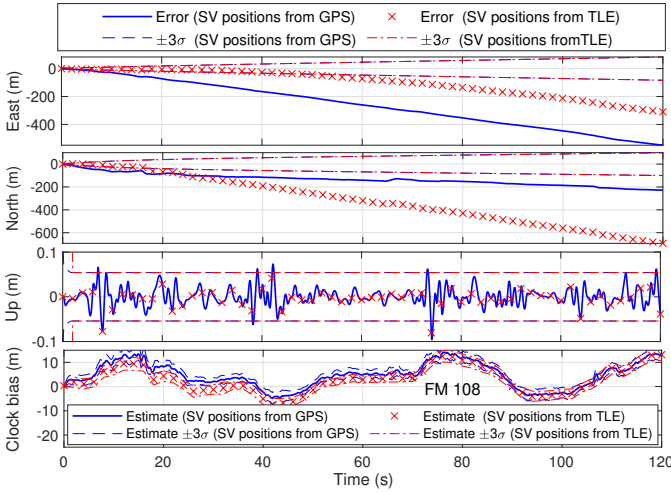


Fig. 15. EKF position estimation error and $\pm 3\sigma$ bounds for non-differential LEO framework. The sigma bounds for the case where SV positions are obtained from GPS and the ones for the case where the SV positions are obtained from TLE files are almost identical.

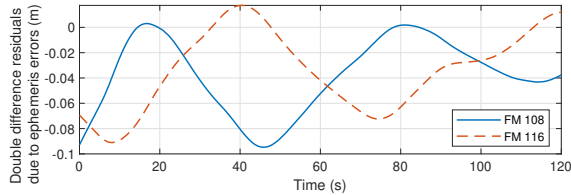


Fig. 16. Double difference residuals due to ephemeris errors for Orbcmm LEO SVs FM 108 and FM 116.

ACKNOWLEDGMENT

The authors would like to thank Dr. Chris Bartone for the insightful discussions and Joshua Morales, MyLinh Nguyen, Ali Abdallah, Mohammad Orabi, Kimia Shamaei, Mahdi Maaref, and Naji Tarabay for their help in data collection.

APPENDIX A DERIVATION OF THE JACOBIAN

$$\text{Define } g_\gamma(\theta_l) \triangleq \frac{\partial \sin[\gamma(\theta_l)]}{\partial \theta_l} = \left[\frac{\sin \theta_l}{\alpha_l \sqrt{1 - \frac{\cos^2 \theta_l}{\alpha_l^2}}} - 1 \right] \cos[\gamma(\theta_l)],$$

$$\begin{aligned} g_{01}^\phi(\phi_l, \theta_l) &\triangleq \frac{\partial f_{01}(\phi_l, \theta_l)}{\partial \phi_l} = \sin \lambda_0 \sin \phi_l - \sin \varphi_0 \cos \lambda_0 \cos \phi_l, \\ g_{01}^\theta(\phi_l, \theta_l) &\triangleq \frac{\partial f_{01}(\phi_l, \theta_l)}{\partial \theta_l} = \frac{\cos \varphi_0 \cos \lambda_0}{\cos^2 \theta_l}, \\ g_{02}^\phi(\phi_l, \theta_l) &\triangleq \frac{\partial f_{02}(\phi_l, \theta_l)}{\partial \phi_l} = -\cos \lambda_0 \sin \phi_l - \sin \varphi_0 \sin \lambda_0 \cos \phi_l, \\ g_{02}^\theta(\phi_l, \theta_l) &\triangleq \frac{\partial f_{02}(\phi_l, \theta_l)}{\partial \theta_l} = \frac{\cos \varphi_0 \sin \lambda_0}{\cos^2 \theta_l}, \\ g_{03}^\phi(\phi_l, \theta_l) &\triangleq \frac{\partial f_{03}(\phi_l, \theta_l)}{\partial \phi_l} = \cos \varphi_0 \cos \phi_l, \\ g_{03}^\theta(\phi_l, \theta_l) &\triangleq \frac{\partial f_{03}(\phi_l, \theta_l)}{\partial \theta_l} = \frac{\sin \varphi_0}{\cos^2 \theta_l}, \\ b_{01}^\phi(\phi_l, \theta_l) &\triangleq \frac{\partial a_{01}(\phi_l, \theta_l)}{\partial \phi_l} = \sin[\gamma(\theta_l)] g_{01}^\phi(\phi_l, \theta_l), \\ b_{01}^\theta(\phi_l, \theta_l) &\triangleq \frac{\partial a_{01}(\phi_l, \theta_l)}{\partial \theta_l} \\ &= g_\gamma(\theta_l) f_{01}(\phi_l, \theta_l) + \sin[\gamma(\theta_l)] g_{01}^\theta(\phi_l, \theta_l), \\ b_{02}^\phi(\phi_l, \theta_l) &\triangleq \frac{\partial a_{02}(\phi_l, \theta_l)}{\partial \phi_l} = \sin[\gamma(\theta_l)] g_{02}^\phi(\phi_l, \theta_l), \\ b_{02}^\theta(\phi_l, \theta_l) &\triangleq \frac{\partial a_{02}(\phi_l, \theta_l)}{\partial \theta_l} \\ &= g_\gamma(\theta_l) f_{02}(\phi_l, \theta_l) + \sin[\gamma(\theta_l)] g_{02}^\theta(\phi_l, \theta_l), \\ b_{03}^\phi(\phi_l, \theta_l) &\triangleq \frac{\partial a_{03}(\phi_l, \theta_l)}{\partial \phi_l} = \sin[\gamma(\theta_l)] g_{03}^\phi(\phi_l, \theta_l), \\ b_{03}^\theta(\phi_l, \theta_l) &\triangleq \frac{\partial a_{03}(\phi_l, \theta_l)}{\partial \theta_l} \\ &= g_\gamma(\theta_l) f_{03}(\phi_l, \theta_l) + \sin[\gamma(\theta_l)] g_{03}^\theta(\phi_l, \theta_l). \end{aligned}$$

Since by definition $\|\mathbf{r}_{1e0,l}\|_2 = \alpha_l R_E$, then the following holds

$$a_{01}^2(\phi_l, \theta_l) + a_{02}^2(\phi_l, \theta_l) + a_{03}^2(\phi_l, \theta_l) = 1. \quad (27)$$

Subsequently, the elements of the jacobian matrix $\mathbf{J}_y(\phi_l, \theta_l)$ are given by

$$\begin{aligned} \frac{\partial \lambda_l}{\partial \phi_l} &\triangleq \frac{b_{02}^\phi(\phi_l, \theta_l) a_{01}(\phi_l, \theta_l) - b_{01}^\phi(\phi_l, \theta_l) a_{02}(\phi_l, \theta_l)}{a_{01}^2(\phi_l, \theta_l) + a_{02}^2(\phi_l, \theta_l)} \\ \frac{\partial \lambda_l}{\partial \theta_l} &\triangleq \frac{b_{02}^\theta(\phi_l, \theta_l) a_{01}(\phi_l, \theta_l) - b_{01}^\theta(\phi_l, \theta_l) a_{02}(\phi_l, \theta_l)}{a_{01}^2(\phi_l, \theta_l) + a_{02}^2(\phi_l, \theta_l)} \\ \frac{\partial \varphi_l}{\partial \phi_l} &\triangleq \frac{b_{03}^\phi(\phi_l, \theta_l)}{\sqrt{a_{01}^2(\phi_l, \theta_l) + a_{02}^2(\phi_l, \theta_l)}} \\ \frac{\partial \varphi_l}{\partial \theta_l} &\triangleq \frac{b_{03}^\theta(\phi_l, \theta_l)}{\sqrt{a_{01}^2(\phi_l, \theta_l) + a_{02}^2(\phi_l, \theta_l)}}, \end{aligned}$$

and the determinant of $\mathbf{J}_y(\mathbf{q}_l)$ is given by

$$|\mathbf{J}_y(\mathbf{q}_l)| = \frac{a_{01}(b_{02}^\phi b_{03}^\theta - b_{02}^\theta b_{03}^\phi) - a_{02}(b_{01}^\phi b_{03}^\theta - b_{01}^\theta b_{03}^\phi)}{(a_{01}^2 + a_{02}^2)^{\frac{3}{2}}}. \quad (28)$$

REFERENCES

- [1] T. Reid, A. Neish, T. Walter, and P. Enge, "Broadband LEO constellations for navigation," *NAVIGATION, Journal of the Institute of Navigation*, vol. 65, no. 2, pp. 205–220, 2018.
- [2] M. Joerger, L. Gratton, B. Pervan, and C. Cohen, "Analysis of Iridium-augmented GPS for floating carrier phase positioning," *NAVIGATION, Journal of the Institute of Navigation*, vol. 57, no. 2, pp. 137–160, 2010.
- [3] K. Pesyna, Z. Kassas, and T. Humphreys, "Constructing a continuous phase time history from TDMA signals for opportunistic navigation," in *Proceedings of IEEE/ION Position Location and Navigation Symposium*, April 2012, pp. 1209–1220.
- [4] J. Morales, J. Khalife, A. Abdallah, C. Ardito, and Z. Kassas, "Inertial navigation system aiding with Orbcomm LEO satellite Doppler measurements," in *Proceedings of ION GNSS Conference*, September 2018, pp. 2718–2725.
- [5] Z. Kassas, J. Morales, and J. Khalife, "New-age satellite-based navigation – STAN: simultaneous tracking and navigation with LEO satellite signals," *Inside GNSS Magazine*, vol. 14, no. 4, pp. 56–65, 2019.
- [6] T. Reid, A. Neish, T. Walter, and P. Enge, "Leveraging commercial broadband LEO constellations for navigating," in *Proceedings of ION GNSS Conference*, September 2016, pp. 2300–2314.
- [7] J. Morales, J. Khalife, and Z. Kassas, "Simultaneous tracking of Orbcomm LEO satellites and inertial navigation system aiding using Doppler measurements," in *Proceedings of IEEE Vehicular Technology Conference*, April 2019, pp. 1–6.
- [8] J. Khalife and Z. Kassas, "Receiver design for Doppler positioning with LEO satellites," in *Proceedings of IEEE International Conference on Acoustics, Speech and Signal Processing*, May 2019, pp. 5506–5510.
- [9] C. Ardito, J. Morales, J. Khalife, A. Abdallah, and Z. Kassas, "Performance evaluation of navigation using LEO satellite signals with periodically transmitted satellite positions," in *Proceedings of ION International Technical Meeting Conference*, 2019, pp. 306–318.
- [10] L. Merry, R. Faragher, and S. Schedin, "Comparison of opportunistic signals for localisation," in *Proceedings of IFAC Symposium on Intelligent Autonomous Vehicles*, September 2010, pp. 109–114.
- [11] A. Dammann, S. Sand, and R. Raulefs, "Signals of opportunity in mobile radio positioning," in *Proceedings of European Signal Processing Conference*, August 2012, pp. 549–553.
- [12] J. del Peral-Rosado, R. Raulefs, J. Lopez-Salcedo, and G. Seco-Granados, "Survey of cellular mobile radio localization methods: from 1G to 5G," *IEEE Communications Surveys & Tutorials*, vol. 20, no. 2, pp. 1124–1148, 2018.
- [13] Z. Kassas, "Collaborative opportunistic navigation," *IEEE Aerospace and Electronic Systems Magazine*, vol. 28, no. 6, pp. 38–41, 2013.
- [14] J. McEllroy, "Navigation using signals of opportunity in the AM transmission band," Master's thesis, Air Force Institute of Technology, Wright-Patterson Air Force Base, Ohio, USA, 2006.
- [15] S. Fang, J. Chen, H. Huang, and T. Lin, "Is FM a RF-based positioning solution in a metropolitan-scale environment? A probabilistic approach with radio measurements analysis," *IEEE Transactions on Broadcasting*, vol. 55, no. 3, pp. 577–588, September 2009.
- [16] A. Popleteev, "Indoor positioning using FM radio signals," Ph.D. dissertation, University of Trento, Italy, 2011.
- [17] P. Thevenon, S. Damien, O. Julien, C. Macabiau, M. Bousquet, L. Ries, and S. Corazza, "Positioning using mobile TV based on the DVB-SH standard," *NAVIGATION, Journal of the Institute of Navigation*, vol. 58, no. 2, pp. 71–90, 2011.
- [18] C. Yang, T. Nguyen, and E. Blasch, "Mobile positioning via fusion of mixed signals of opportunity," *IEEE Aerospace and Electronic Systems Magazine*, vol. 29, no. 4, pp. 34–46, April 2014.
- [19] R. Faragher and R. Harle, "Towards an efficient, intelligent, opportunistic smartphone indoor positioning system," *NAVIGATION, Journal of the Institute of Navigation*, vol. 62, no. 1, pp. 55–72, 2015.
- [20] J. Khalife, Z. Kassas, and S. Saab, "Indoor localization based on floor plans and power maps: Non-line of sight to virtual line of sight," in *Proceedings of ION GNSS Conference*, September 2015, pp. 2291–2300.
- [21] C. Gentner, T. Jost, W. Wang, S. Zhang, A. Dammann, and U. Fiebig, "Multipath assisted positioning with simultaneous localization and mapping," *IEEE Transactions on Wireless Communications*, vol. 15, no. 9, pp. 6104–6117, September 2016.
- [22] W. Xu, M. Huang, C. Zhu, and A. Dammann, "Maximum likelihood TOA and OTDOA estimation with first arriving path detection for 3GPP LTE system," *Transactions on Emerging Telecommunications Technologies*, vol. 27, no. 3, pp. 339–356, 2016.
- [23] K. Shamaei, J. Khalife, and Z. Kassas, "Exploiting LTE signals for navigation: Theory to implementation," *IEEE Transactions on Wireless Communications*, vol. 17, no. 4, pp. 2173–2189, April 2018.
- [24] J. Khalife and Z. Kassas, "Navigation with cellular CDMA signals – part II: Performance analysis and experimental results," *IEEE Transactions on Signal Processing*, vol. 66, no. 8, pp. 2204–2218, April 2018.
- [25] C. Gentner, "Channel-SLAM: Multipath assisted positioning," Ph.D. dissertation, Ulm University, 2018.
- [26] Z. Kassas, J. Khalife, K. Shamaei, and J. Morales, "I hear, therefore I know where I am: Compensating for GNSS limitations with cellular signals," *IEEE Signal Processing Magazine*, pp. 111–124, September 2017.
- [27] T. Kang, H. Lee, and J. Seo, "TOA-based ranging method using CRS in LTE signals," *Journal of Advanced Navigation Technology*, vol. 23, no. 5, pp. 437–443, October 2019.
- [28] J. Khalife and Z. Kassas, "Precise UAV navigation with cellular carrier phase measurements," in *Proceedings of IEEE/ION Position, Location, and Navigation Symposium*, April 2018, pp. 978–989.
- [29] J. Khalife, K. Shamaei, S. Bhattacharya, and Z. Kassas, "Centimeter-accurate UAV navigation with cellular signals," in *Proceedings of ION GNSS Conference*, September 2018, pp. 2321–2331.
- [30] K. Shamaei and Z. Kassas, "Sub-meter accurate UAV navigation and cycle slip detection with LTE carrier phase," in *Proceedings of ION GNSS Conference*, September 2019, pp. 2469–2479.
- [31] D. Lawrence, H. Cobb, G. Gutt, M. O'Connor, T. Reid, T. Walter, and D. Whelan, "Navigation from LEO: Current capability and future promise," *GPS World Magazine*, vol. 28, no. 7, pp. 42–48, July 2017.
- [32] J. Khalife and Z. Kassas, "Assessment of differential carrier phase measurements from orbcomm LEO satellite signals for opportunistic navigation," in *Proceedings of ION GNSS Conference*, September 2019, pp. 4053–4063.
- [33] K. Pesyna, T. Humphreys, R. Heath, T. Novlan, and J. Zhang, "Exploiting antenna motion for faster initialization of centimeter-accurate GNSS positioning with low-cost antennas," *IEEE Transactions on Aerospace and Electronic Systems*, vol. 53, no. 4, pp. 1597–1613, August 2017.
- [34] P. Misra and P. Enge, *Global Positioning System: Signals, Measurements, and Performance*, 2nd ed. Ganga-Jamuna Press, 2010.
- [35] P. J. G. Teunissen, "The least-squares ambiguity decorrelation adjustment: a method for fast gps integer ambiguity estimation," *Journal of Geodesy*, vol. 70, no. 1, pp. 65–82, November 1995.
- [36] K. Crowe and R. Raines, "A model to describe the distribution of transmission path elevation angles to the Iridium and Globalstar satellite systems," *IEEE Communications Letters*, vol. 3, no. 8, pp. 242–244, Aug 1999.
- [37] S. L. and C. Liu, "An analytical model to predict the probability density function of elevation angles for LEO satellite systems," *IEEE Communications Letters*, vol. 6, no. 4, pp. 138–140, April 2002.
- [38] Z. Kassas, P. Clossas, and J. Gross, "Navigation systems for autonomous and semi-autonomous vehicles: Current trends and future challenges," *IEEE Aerospace and Electronic Systems Magazine*, vol. 34, no. 5, pp. 82–84, May 2019.
- [39] SpaceX, "FCC File Number: SATMOD2018110800083," *IB FCC Report*, November 2018, accessed: November 29, 2018.
- [40] P. Teunissen, "Success probability of integer gps ambiguity rounding and bootstrapping," *Journal of Geodesy*, vol. 72, pp. 606–612, 1998.
- [41] J. Vetter, "Fifty years of orbit determination: Development of modern astrodynamics methods," *Johns Hopkins APL Technical Digest*, vol. 27, no. 3, pp. 239–252, November 2007.
- [42] J. Morales and Z. Kassas, "Information fusion strategies for collaborative radio SLAM," in *Proceedings of IEEE/ION Position Location and Navigation Symposium*, April 2018, pp. 1445–1454.
- [43] Z. Kassas and T. Humphreys, "Observability analysis of collaborative opportunistic navigation with pseudorange measurements," *IEEE Transactions on Intelligent Transportation Systems*, vol. 15, no. 1, pp. 260–273, February 2014.
- [44] Z. Kassas, V. Ghadiok, and T. Humphreys, "Adaptive estimation of signals of opportunity," in *Proceedings of ION GNSS Conference*, September 2014, pp. 1679–1689.